Design methodology for efficient frequency conversion in Bragg reflection lasers

Bhavin J. Bijlani[1] and Amr S. Helmy[1,*]

Edward S. Rogers Sr. Department of Electrical and Computer Engineering, University of Toronto, 10 King's College Road, Toronto, Ontario M5S 3G4, Canada
**Corresponding author: a.helmy@utoronto.ca*

Received April 17, 2012; revised July 1, 2012; accepted July 9, 2012;
posted July 10, 2012 (Doc. ID 166805); published August 23, 2012

Bragg reflection waveguides are shown to be structures that can enable the integration of a laser and optically nonlinear medium within the same cavity for efficient frequency conversion. An effective and simple method of designing phase-matched laser structures utilizing transfer matrix analysis is described. The structures are first optimized in terms of laser performance and then for enhancement of $\chi^{(2)}$ nonlinearity. The method for optimization shows that designing for either optimum laser performance or optimum nonlinear performance can conflict. An efficiency term encompassing the requirements of both the laser and nonlinear element is derived. This serves as a figure of merit that includes parameters relevant to both the laser and the nonlinear device. It is then utilized to optimize the structure for efficient parametric conversion. This figure of merit is extended to examine parametric oscillation in the laser cavity for both singly resonant and doubly resonant configurations. It is found that threshold values of 4 W in a practical device can be obtained. Such power levels are easily obtained by mode locking the pump laser. With reduced propagation loss through etch and design improvement, sub-Watt thresholds can be realized.

OCIS codes: 130.5296, 130.3120, 140.2020, 190.5970, 190.4410, 230.1480.

1. INTRODUCTION

Compact tunable sources of coherent optical radiation are of great benefit for many applications, such as sensing, spectroscopy, and communications. In wavelength regimes where suitable materials for tunable laser sources are not available, the use of nonlinear frequency mixing to generate the desired wavelengths is a popular alternative. With the advent of optical parametric oscillators (OPOs), tunable radiation well into the mid-IR is readily available in both CW and pulsed settings. The availability of these devices can be largely attributed to the development of high-quality nonlinear materials, such as periodically poled lithium niobate (PPLN) and periodically poled potassium titanyl phosphate (PPKTP). These nonlinear materials have demonstrated large parametric gain, wide phase-matching bandwidth, and low optical losses. Nonetheless, OPOs built using these materials are not rugged or mobile. This is because they have stringent restrictions on alignment and are typically operated in locations with low levels of vibration.

The use of an all-semiconductor integrated platform to implement OPOs is an attractive alternative to overcome the above-mentioned shortcomings [1]. Compound III–V semiconductors, such as AlGaAs or InGaAsP, can offer many advantages as the integration platform. For example, AlGaAs is transparent well into the mid-IR (≈17 μm), has relatively large second-order nonlinearity, established growth, and mature fabrication technology. These structures can also support cascaded $\chi^{(2)}$ in a similar fashion to what has been already reported in other materials, such as PPLN [2]. In contrast, semiconductors require high peak power and, hence, short pulse operation of the pump laser to obtain high efficiency.

Several techniques to phase match second-order nonlinearities in semiconductors have been reported in the past [3]. These range from quasi-phase-matching using growth on patterned substrates and domain disordering, to the use of form birefringence and M-shaped waveguides. The most promising of these technologies utilize form birefringence to achieve phase matching. Using this technique, OPO thresholds below 100 mW were predicted [4]. However, it has not been possible thus far to integrate the nonlinear sections with on-chip diode lasers and thus monolithic OPO devices have not been realized. As such, the development of compact, robust optical parametric devices remains a topic of active research.

Recently, the use of Bragg reflection waveguides (BRWs) as a means of phase matching second-order nonlinearity [5] has shown high conversion efficiencies in both short pulse [6] and CW [7] second-harmonic generation (SHG). Conversion efficiency over 10,000%/W cm^2 was achieved using picosecond pulses. Further, the BRW waveguide is extremely dispersive and affords unprecedented tunability of the phase matching with bandwidth in excess of 60 nm demonstrated in the sum frequency generation configuration [8] and 100 nm in difference frequency generation (DFG) [9]. Diode lasers where lasing takes place through the fundamental Bragg mode have also been investigated [10] and demonstrated [11]. These developments strongly indicate that BRW structures are a promising platform for monolithically integrated parametric devices, such as OPOs and self-pumped frequency conversion devices.

This paper will examine the trade-offs and optimization methodology associated with designing phase-matched BRW diode lasers that are aimed at three-wave mixing for DFG and parametric oscillation within the laser cavity. Parametric oscillation is more favorable as a means of producing coherent radiation in comparison to DFG as it provides higher

output power and needs only one pump laser source. In this device, both the pump laser and the nonlinear medium coexist in the same waveguide and cavity. A schematic of an electrically pumped OPO based on AlGaAs BRW is shown in Fig. 1. Here, the waveguide core is surrounded by Bragg reflectors above and below. The reflector above is p-doped, the reflector below is n-doped, while the core is left intrinsic. At the center of the core is a set of quantum wells to produce the desired pump wavelength through electrical injection.

In this work, the active region used will utilize an InGaAs quantum well (QW) with GaAs barriers lasing at $\lambda_p = 980$ nm for the pump source. This wavelength is chosen due to the availability of a mature technology for producing high-power diode lasers at this wavelength [12]. The pump interacts with the nonlinearity of the semiconductor crystal to generate a signal at $\lambda_s = 1550$ nm and an idler at $\lambda_i = 2665$ nm. Many optical communication sources and amplifiers, such as InGaAsP diode lasers and erbium-doped fiber amplifiers, exist at this signal wavelength. Also, absorption bands for water and several carbon bonds lie in the wavelength range encompassing 2–3 μm [13], thus making 2665 nm a useful idler wavelength for sensing applications.

The forthcoming sections are organized as follows: A method of modal analysis of BRW lasers and the design rules needed to obtain efficient nonlinear conversion in the waveguide is first put forward. Optimization of either component alone can lead to poor performance for the device as a whole. As such, a device performance parameter is essential for effective design and optimization. This will, in turn, enable the optimization of both functionalities simultaneously in an integrated semiconductor platform. A suitable parameter that encompasses the attributes of both the pump and the nonlinear performance is derived and discussed. It is then used to analyze these structures to determine suitable OPO (pump laser + nonlinear conversion) device parameters to obtain practical oscillation threshold.

2. PHASE-MATCHED BRW LASER STRUCTURES

A BRW can be described as a one-dimensional structure containing a core layer surrounded on either side by transverse Bragg reflectors (TBRs). Through appropriate design, an optical mode can propagate with low loss along the waveguide via Bragg reflection [14]. A class of BRWs known as matching-layer enhanced BRW (BRW-ML) has recently been developed for efficient frequency conversion [15]. By placing a defect layer at the interface of the core and TBR, the Bragg mode field profile can be tailored to provide better spatial overlap among the optical modes involved in the nonlinear process. This enhancement in the overlap between the modes involved increases the conversion efficiency and has recently resulted in some of the highest SHG conversion reported in AlGaAs waveguides. A schematic of a typical BRW-ML is shown in Fig. 2(a). This work will utilize BRW-MLs for the frequency conversion, although the methodology is universal to other classes of BRWs.

A QW placed within this structure would allow for gain of the Bragg mode. Recently, a BRW diode laser with uncoated facets was demonstrated [11,16], where ≈100 mW optical power was generated in the Bragg mode. Powers greater than this are not unusual for diode lasers and the internal power can far exceed this depending on the mirror reflectivities. By appropriately designing the BRW cavity, the high field strength can be utilized for frequency conversion. This method of integration is monolithic and advantageous compared to other techniques. For example, the device is naturally aligned and there is no need for complex fabrication of two separate sections (one for lasing, the other for nonlinear conversion). This intracavity method is thus appealing as a low cost, low complexity solution to all-semiconductor parametric devices.

A. Phase-Matching $\chi^{(2)}$ Processes

Nonlinear frequency conversion requires a formidable control over the modal effective indices for phase matching. Although there have been many techniques developed to compute BRW effective indices [14,17], most have assumed a single layer core. Diode lasers however, have additional layers in the core region, namely, the QWs and barriers. Because of the dispersive nature of Bragg modes, the presence of the active region composed of many dielectric layers cannot be ignored in the modal analysis. As such, a generic field transfer matrix approach known as the transverse resonance condition (TRC)

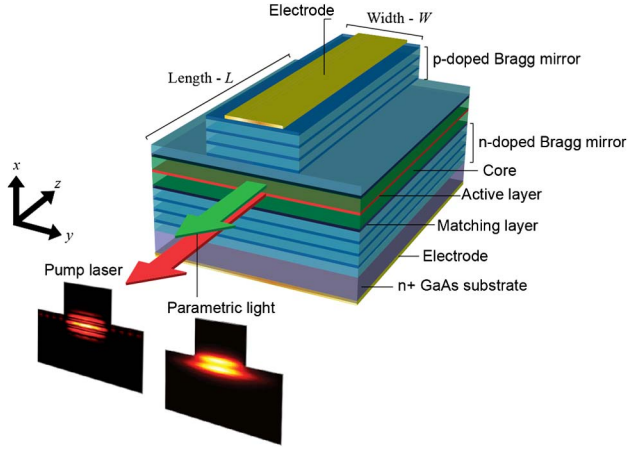

Fig. 1. (Color online) Schematic of an edge-emitting ridge BRW laser with its cavity phase matched for $\chi^{(2)}$ processes. Current injection generates the pump laser, which propagates as the Bragg mode. Through the nonlinearity of the semiconductor, parametric light is generated within the laser cavity and propagates as a bound mode.

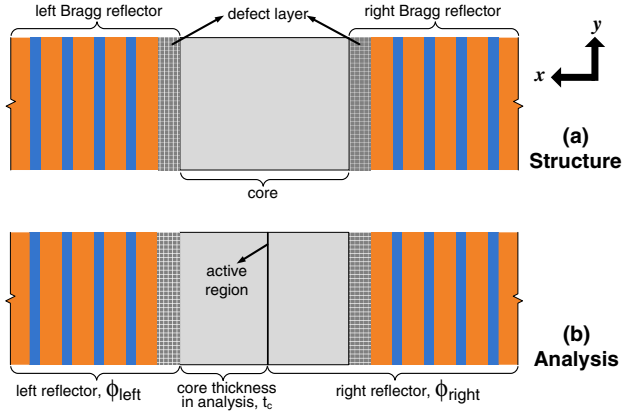

Fig. 2. (Color online) (a) Schematic of a BRW-ML. A core layer is surrounded by two transverse Bragg reflectors with a defect layer, referred to as matching layer, in between. (b) Technique used to analyze BRW-ML structures with active region layers. The right reflector contains the active region, while the core is only the left half. The reflection ϕ_{right} now includes the active region.

[18] is utilized, shown as (1). TRC is derived using a simple ray optics treatment for the propagation of optical modes in waveguides. It uses the fact that a guided mode is formed within the waveguide when the transverse field profile of the mode establishes a standing wave. Mathematically, the transverse resonance condition can be expressed as

$$2t_c\sqrt{k_c^2-\beta^2}+\phi_{\text{left}}+\phi_{\text{right}}=\frac{4\pi n_{\text{eff}}t_c}{\lambda_i}+\phi_{\text{left}}+\phi_{\text{right}}=2m\pi, \tag{1}$$

where t_c is the thickness of the core, m is the order of the Bragg mode, k_c is the wavevector inside the core, β is the propagation constant, n_{eff} is the effective mode index, λ_i is the wavelength in free space, and ϕ_{left} and ϕ_{right} are the phases induced due to reflection from the left and right mirrors, respectively. Compared to Fig. 2(a), the structure is redefined as shown in Fig. 2(b) to include the core region for modal analysis. The active region and right half of the core are now considered part of the right Bragg reflector. The left half of the original core is treated as the new core. This interpretation of the structure now includes the dispersive contribution of the active region layers. The phase terms can be determined by computing the reflectivity of each mirror at a given angle θ where $\sin(\theta)=n_{\text{eff}}/n_c$ with n_c denoting the refractive index of the core. Using the 2×2 transfer matrix of the mirror, M with elements $M_{1,1},\ldots,M_{2,2}$, the complex reflectivity, r, and the reflection phase shift, ϕ, can be found as

$$r=-\frac{M_{2,1}}{M_{1,1}}=|r|e^{i\phi}. \tag{2}$$

Consider the downconversion process, where a pump at an angular frequency of ω_p generates a signal at ω_s and an idler at ω_i. Using BRWs, the pump mode propagates as a Bragg mode, while both signal and idler are bound modes with their propagation relying on total internal reflection (TIR). Conservation of energy then requires that $\omega_p-\omega_s-\omega_i=0$. For efficient nonlinear conversion, the conservation of linear momentum requires perfect phase matching to be satisfied such that $\Delta\beta=\beta_p-\beta_s-\beta_i=0$, where β_p, β_s, and β_i are the propagation constants of pump, signal, and idler, respectively.

For a QW laser diode, such as the one shown in Fig. 1, the polarization state of the lasing mode is TE polarization. As such, we focus on yjr Type II downconversion process in AlGaAs with a TE-polarized pump, a TM-polarized signal, and a TE-polarized idler. This results in the Type II phase-matching condition expressed as

$$\Delta\beta=2\cdot\pi\cdot\left(\frac{n^{\text{TE}}_{\text{eff};p,\text{BRW}}}{\lambda_p}-\frac{n^{\text{TM}}_{\text{eff};s,\text{TIR}}}{\lambda_s}-\frac{n^{\text{TE}}_{\text{eff};i,\text{TIR}}}{\lambda_i}\right)=0. \tag{3}$$

Fundamental modes are chosen due to low propagation losses, lower beam divergence, and better overlap for nonlinear conversion. To compute the required effective indices of signal and idler in Eq. (3), another transfer matrix method is used [19]. For a given layered structure, the fundamental TIR modal effective index can be found by sweeping all possible values from $\min\{n_j\}$ to $\max\{n_j\}$, where $\{n_j\}$ refers to the set containing refractive indices of all existing layers within the structure.

To demonstrate the technique of finding a phase-matched BRW-ML laser structure, some representative initial parameters will be used. This design is chosen as a starting point because it has a relatively strong nonlinear conversion, which will be detailed further in Section 3. As mentioned before, the pump wavelength is 980 nm, the signal wavelength is 1550 nm, and the idler is 2665 nm. Our choice of material system will be $Al_xGa_{1-x}As$. In diode lasers, it is beneficial to utilize low aluminum values to improve the active device performance. Further, at $x\approx0.45$, the bandgap becomes indirect and DX-center defects can be present while dopant activation is also reduced [20]. Thus, the TBR materials chosen are $x_1=0.15$ and $x_2=0.40$ for the high and low index layers, respectively with five periods above and below. The defect-layer material is $x_m=0$, the core is $x_c=0.1$ with a thickness of $t_c=600$ nm. This structure will be referred to as Design A. By varying the defect-layer thickness t_m and computing the effective indices of the pump, signal, and idler, the nonlinear phase mismatch $\Delta\beta$ can be monitored, as shown in Fig. 3. Note the defect-layer thickness for phase matching is quite different when a QW with barriers is included in the modal analysis using the transfer matrix method.

As can be seen from Fig. 3, a choice of $t_m=87.3$ nm for the defect-layer thickness allows for a phase-matched structure of the given three-wave-mixing scenario. In the calculations above, a single $In_{0.2}Ga_{0.8}As$ QW of thickness 6 nm surrounded by 10 nm GaAs barriers is placed in the center of the core. This simulation has also taken material dispersion into consideration, as the variation is significant at the wavelength of the pump, which is 980 nm. The AlGaAs material refractive indices are found using the model developed by Gehrsitz *et al.* [21]. The $In_{0.2}Ga_{0.8}As$ QW refractive indices are computed using the binary values from GaAs and InAs and interpolated to the ternary alloy [22]. The relevant field profiles are shown in Fig. 4. The profiles in Fig. 4(a) and 4(b) are the profiles of the Bragg mode and fundamental TIR mode at the pump wavelength. This allows us to compare the two modes at the laser wavelength. Figures 4(c) and 4(d) show the field profiles of the fundamental TIR modes at the signal and idler wavelengths. The refractive index profile of Design A for the three wavelengths are shown in Fig. 5. Modal indices are highlighted on the profiles by a horizontal line to show how they line up with the material indices. Subsection 2.B will detail how to modify this phase-matched design for improved laser operation.

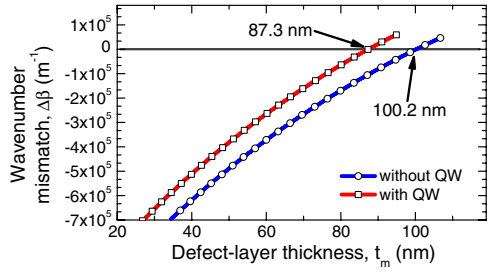

Fig. 3. (Color online) Index mismatch $\Delta\beta$ for BRW-ML Design A as a function of the defect-layer thickness when the QW active region is ignored (squares) in mode calculations and when the QW is included (circles).

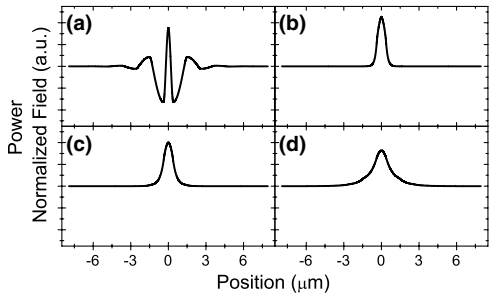

Fig. 4. Field profiles for the relevant modes of Design A: (a) BRW E_y and (b) TIR E_y at $\lambda_p = 980$ mm; (c) the TIR H_y at $\lambda_s = 1550$ mm and (d) TIR E_y at $\lambda_i = 2665$ mm. Profiles have been normalized to power for comparison.

B. Laser Cavity Design

As shown in the previous section, the QW can have a significant impact on the nonlinear performance if ignored. The important consideration for lasing is the spatial overlap between the QW and Bragg mode. For larger modal gain and, hence, lower threshold gain, this spatial overlap must be larger than that of any other guided mode in the structure. However, as can be seen in Fig. 4(b), the fundamental TIR mode is also confined to the core region with a peak at the center. It is, therefore, unlikely the Bragg mode will have higher laser gain and Design A would not be able to operate as a BRW laser (i.e., lasing in the BRW mode).

A quantity that quantifies the spatial overlap between the QW and the lasing mode is the overlap factor, Γ_i, which is defined as

$$\Gamma_i = \frac{\int_{-d/2}^{d/2} |E_i|^2 \mathrm{d}x}{\int_{-\infty}^{\infty} |E_i|^2 \mathrm{d}x}, \tag{4}$$

where d is the thickness of the QW region. If multiple QWs exist, then this parameter is the summation of overlap with each QW. Suppose a single InGaAs QW, as defined in Subsection 2.A, is placed in the center of the core in Design A. Using Eq. (4), the overlap factor for the Bragg and TIR modes are $\Gamma_{\mathrm{BRW}}^{(\mathrm{TE})}(980\ \mathrm{nm}) = 0.55\%$ and $\Gamma_{\mathrm{TIR}}^{(\mathrm{TE})}(980\ \mathrm{nm}) = 1.13\%$, respectively. These values imply that Design A cannot be employed for Bragg mode lasing because the TIR mode has higher overlap with the QW.

There are two techniques to improve $\Gamma_{\mathrm{BRW}}^{(\mathrm{TE})}$, both of which create a dip in the TIR mode while maintaining a peak in the profile of the Bragg mode at the center of the core, essentially engineering the field profile. First, the index of the core layer can be reduced to a point, where it is the lowest index of the structure. This results in TIR modes that are dual lobed in nature with peaks at each defect layer and minimum at the core center. The benefit of this approach is reflected in a favorable overlap ratio between the BRW and TIR modes, as shown in Fig. 6(a). Starting with Design A, the core aluminum fraction is slowly increased (or equivalently its refractive index is decreased). The ratio of $\Gamma_{\mathrm{BRW}}^{(\mathrm{TE})}$ and $\Gamma_{\mathrm{TIR}}^{(\mathrm{TE})}$ steadily increases from 0.78 to 24.4 at $x_c = 0.45$, which is selected as the first optimization point. As justified earlier, we choose not to use aluminum fraction beyond 45%.

Next, the core thickness can be increased to further reduce the TIR field strength at the QW location, allowing the field to decay further from the peak. This is shown as open squares in Fig. 6(a). As core thickness increases, the Γ ratio can be increased to a peak value of 36.3 with $\Gamma_{\mathrm{BRW}}^{(\mathrm{TE})}(980\ \mathrm{nm}) = 1.18\%$ and $\Gamma_{\mathrm{TIR}}^{(\mathrm{TE})}(980\ \mathrm{nm}) = 0.027\%$. This enhanced design will be called Design B and is a 46× increase in the Γ ratio compared to Design A. Design B field profiles are shown in Fig. 7, where the dip at the QW location is readily visible for the TIR E_y at $\lambda_p = 980$ nm. The refractive index profiles of Design B for the three wavelengths are shown in Fig. 8. Here, the mode index of the TIR at the pump is found to be higher than the material index in the core of the waveguide. For Design A, the mode index is lower than the material index in the same region. This is the cause of the dip in pump, signal, and idler TIR field profiles for Design B and not Design A. The beneficial result of this dip is a reduced Γ factor for the TIR mode with respect to the BRW mode.

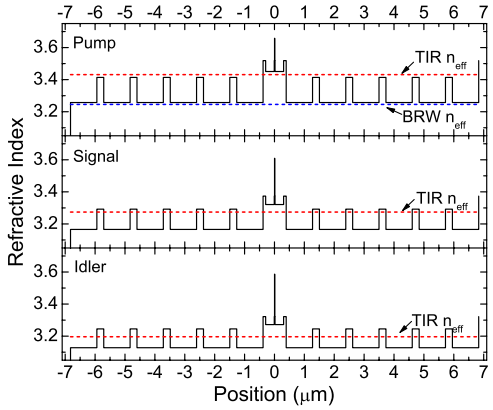

Fig. 5. (Color online) Refractive index profiles of Design A for the (a) pump wavelength, (b) signal wavelength, and (c) idler wavelength.

Another important consideration is the modal propagation loss, α. Because of its leaky nature, Bragg mode leakage to the substrate can become significant. However, it has been shown in the past that such losses can be drastically reduced to practical levels. In our recent demonstration of a BRW laser, the propagation loss was directly measured as 14 cm^{-1} at the lasing wavelength [11], a reasonable value given that the ridge waveguide was deeply etched. Several methods for calculating the Bragg mode loss have been developed. This paper will use the transfer matrix technique developed by Dasgupta *et al.* [23].

Since the laser will pump the nonlinear conversion process, it is essential to examine the laser output power. Typically, the output power of a diode laser is estimated by using self-consistent coupled rate equations. However, for a

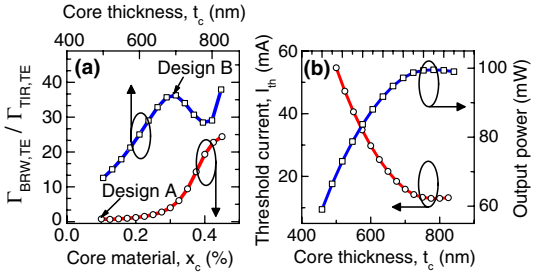

Fig. 6. (Color online) (a) Variation of the ratio $\Gamma_{\mathrm{BRW}}^{(\mathrm{TE})}/\Gamma_{\mathrm{TIR}}^{(\mathrm{TE})}$ with respect to core material (circles) and core thickness (squares). (b) Variation of the threshold current (circles) and output power at 100 mA (squares) with respect to the core thickness.

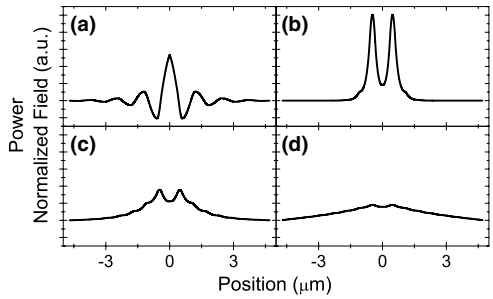

Fig. 7. Field profiles for the relevant modes of Design B: (a) BRW E_y and (b) TIR E_y at λ_p; (c) the TIR H_y at λ_s and (d) TIR E_y at λ_i. Profiles have been normalized to power for comparison.

sufficiently accurate estimation of the output power, a simpler, quasi-phenomenological approach is used that takes into account the variation in Γ and α of a structure and computes the resulting effect on the laser performance. Using such an approach, the laser output power, $P_{\text{out}}(J)$, and threshold current, I_{th} can be determined as

$$P_{\text{out}}(J) = \frac{WL\eta_i}{\lambda_p}\left[J - J_{\text{tr}}\exp\left(\frac{\alpha_p L - \ln(R_{p,1}R_{p,2})}{G_0\Gamma_p L}\right)\right] \times \frac{hc}{e}\frac{\ln(R_{p,1}R_{p,2})}{\ln(R_{p,1}R_{p,2}) - \alpha_p L},$$
$$I_{\text{th}} = \frac{WL\eta_i}{\lambda_p}\frac{hc}{e}J_{\text{tr}}\exp\left(\frac{\alpha_p L - \ln(R_{p,1}R_{p,2})}{G_0\Gamma_p L}\right), \quad (5)$$

where $R_{p,1}$ and $R_{p,2}$ are the facet reflection constants at the pump wavelength, L is the cavity length, W is the injection width, η_i is the internal efficiency, G_0 is material gain, and J_{tr} is the transparency current density. The constants h, c, and e are Plancks constant, the speed of light, and the charge of an electron, respectively. The current I and current density J are related by $I = JWL$. Here, the injection width W is assumed to be the ridge width; a reasonable assumption considering the QW location relative to the etch depth for these waveguides. Detailed derivation of Eq. (5) is discussed in Appendix A.

Some representative values for these laser parameters are given in Table 1. The various phase-matched BRW-ML structures can now be compared in terms of laser performance. For

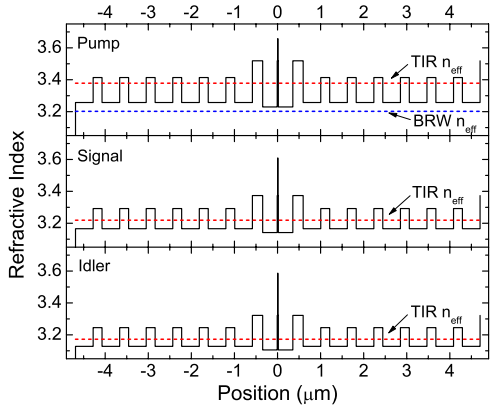

Fig. 8. (Color online) Refractive Index profiles of Design B for the: (a) pump wavelength; (b) signal wavelength and (c) idler wavelength.

Table 1. Typical Laser Parameters Used for Calculations

η_i [%]	α_p [cm^{-1}]	$R_{p,1}$	$R_{p,2}$	J_{tr} [A/cm^2]	L [mm]	W [μm]	G_0 [cm^{-1}]
90	14	0.3	0.3	50	1	4	1000

example, Fig. 6(b) demonstrates how changing the core thickness with $x_c = 0.45$ will affect the laser threshold, which is shown as circles. The output power of the laser, chosen at an arbitrary current (above threshold) of 100 mA is shown as squares. From the figure, there is a wide variation in performance due to structural variations with threshold current varying from 10 mA up to 55 mA.

3. OPTIMIZING THE NONLINEAR INTERACTION

Section 2 explored the optimization of the BRW-ML structure for lasing, but did not include any nonlinear characteristics. Efficient nonlinear conversion is also dependent on modal field profiles and propagation losses, though not necessarily beneficial to the lasing performance. A balance is required between laser design and nonlinear conversion design. This section will detail how to redesign the structures from Section 2 to optimize the conversion process using just a single parameter which takes into account all elements.

In nonlinear optics, several measures are available to compare the efficacy of different structures. Of relevance to this work, the second-order nonlinear effective area, $A_{\text{eff}}^{(2)}$, and the effective structural nonlinear coefficient, d_{eff}, are important parameters [24]. The former contains the overlap of the various interacting mode profiles and the latter averages the bulk nonlinearity, weighted by the field profiles. The equations for both are as follows:

$$d_{\text{eff}} = \frac{\left|\iint_{-\infty}^{+\infty} E_p E_s E_i d(x,y)\mathrm{d}x\mathrm{d}y\right|}{\left|\int_{-\infty}^{+\infty} E_p E_s E_i \mathrm{d}x\mathrm{d}y\right|}, \quad (6a)$$

$$A_{\text{eff}}^{(2)} = \frac{\iint_{-\infty}^{+\infty} E_p^2\mathrm{d}x\mathrm{d}y \iint_{-\infty}^{+\infty} E_s^2\mathrm{d}x\mathrm{d}y \iint_{-\infty}^{+\infty} E_i^2\mathrm{d}x\mathrm{d}y}{\left(\iint_{-\infty}^{+\infty} E_p E_s E_i\mathrm{d}x\mathrm{d}y\right)^2}. \quad (6b)$$

To compute d_{eff}, the bulk nonlinear constant for each material, $d(x,y)$, is used as measured by Ohashi *et al.* [25]. The fields required in both equations are two-dimensional transverse profiles. A simple method to compute these is via the effective-index approximation [26]. Here, ridge waveguides of width 4 μm are assumed. Utilizing these parameters, an equation for conversion efficiency will be derived using the nonlinear coupled mode equations. Under the approximation of no pump depletion, perfect phase matching, and weak conversion, for a DFG process where A_s is much larger than A_i, the coupled mode equations are defined as

$$\frac{\partial A_p}{\partial z} = i\frac{\kappa}{\lambda_p}A_s A_i - \frac{\alpha_p}{2}A_p \approx 0, \quad (7a)$$

$$\frac{\partial A_s}{\partial z} = -i\frac{\kappa}{\lambda_s}A_p A_i^* - \frac{\alpha_s}{2}A_s \approx -\frac{\alpha_s}{2}A_s, \quad (7b)$$

$$\frac{\partial A_i}{\partial z} = -i\frac{\kappa}{\lambda_i}A_p A_s^* - \frac{\alpha_i}{2}A_i, \tag{7c}$$

$$\kappa = \frac{4\pi d_{\text{eff}}}{\sqrt{2c\epsilon_0 n_{\text{eff},p} n_{\text{eff},s} n_{\text{eff},i} A_{\text{eff}}^{(2)}}}, \tag{7d}$$

where $A_j, j \in \{p, s, i\}$, is the envelope amplitudes and normalized such that $P_j = |A_j|^2$. Eq. (7b) is simplified by ignoring the first term (nonlinear component) because $A_i \ll A_s$ in the weak conversion regime.

Further, Eq. (7a) is simplified to zero because of laser gain clamping above threshold. In diode lasers, the threshold occurs when the optical gain equals the losses and maintains this above the threshold current. For the laser, the conversion to the signal or idler is considered a "loss" and will be immediately compensated by a slight increase in the slope efficiency and threshold. Therefore, even if there is pump depletion above threshold due to efficient frequency conversion taking place within the diode cavity, the photon density will be replenished to remain constant at equilibrium across the cavity. This pump depletion will only take place at higher injection regime above threshold, where the pump powers are significant enough to induce efficient conversion and, hence, pump depletion. The observed behavior will be a reduction in the slope efficiency in this regime. In the weak conversion regime, this loss of laser power results in a negligible increase in laser threshold or slope efficiency at a given current; a valid assumption, since the laser gain is several orders stronger than the nonlinear gain. As such, we believe the pump propagation loss can be ignored in the analytical equations as the photon density in the cavity will remain constant.

The solution to these equations can readily be found as

$$A_p(z) = A_p(0), \tag{8a}$$

$$A_s(z) = A_s(0)\exp(-\alpha_s z/2), \tag{8b}$$

$$A_i(z) = -i\frac{\kappa}{\lambda_i}A_s^*(0)A_p^*(0)\exp(-\alpha_i z/2)\frac{\exp[-(\alpha_s+\alpha_i)z/2]}{(\alpha_s+\alpha_i)/2}. \tag{8c}$$

The boundary conditions for Eq. (8) are $A_p(z) = A_p(0)$ and $A_i(0) = 0$. Using these formulas, the conversion efficiency, η, can be derived as

$$\eta = \frac{P_i}{P_p P_s} = \frac{|\kappa|^2 L^2}{\lambda_i^2}\exp[-(\alpha_s+\alpha i)L/2]\frac{\sinh^2([\alpha_s-\alpha_i]L/4)}{([\alpha_s-\alpha_i]L/4)^2}, \tag{9a}$$

$$\eta' = \eta \cdot P_{p,\text{internal}}. \tag{9b}$$

Equation (9a) for η is the traditional efficiency term in that it describes the rate of conversion with respect to input signal or pump power. It takes into account both nonlinear terms d_{eff} and $A_{\text{eff}}^{(2)}$ but does not take into account any laser parameters, such as Γ and α_p. In order to address this, a second efficiency parameter, η', is defined in Eq. (9b) whereby the estimated laser power is used as the input pump power. Here, $P_{p,\text{internal}} = P_p/\sqrt{T_{p,1}T_{p,2}}$, where P_p is the estimated average output power of the laser as shown in Subsection 2.B and $T_{p,1}$ and $T_{p,2}$ are the transmission coefficients. As such, η' is the rate of conversion of the input signal power for a given laser structure at a given laser operating point. This efficiency term includes all the relevant laser and nonlinear parameters described previously and is, thus, a valid figure of merit as an optimization parameter.

To calculate both η and η', first the signal and idler losses must be estimated. We rely on experimental data of the TIR mode in a similar BRW-ML structure where loss values of TE- and TM-polarized TIR mode around 1550 nm were measured to be ≈2.0 cm^{-1}. Since AlGaAs does not contain any strong absorption up to the mid-IR, modal propagation losses would not be significantly different at the idler wavelength. Thus, the efficiency calculated here will use this value for the idler and signal losses. It should be noted that the idler mode is less confined in the core and would, therefore, extend more into the bottom cladding. This will result in it experiencing a stronger leakage loss component in comparison to the signal and pump. This leakage is into the high-index GaAs substrate and is present but typically small (<0.01 cm^{-1}) for most modes. The idler leakage contribution is not likely to be dominant because the side-wall scattering is typically the most significant source of loss in these ridge waveguides.

The relative efficiencies with respect to core thickness are shown in Fig. 9. Note the assumptions detailed in Table 1 are again utilized. Here, the peak in η' occurs at a core thickness of 670 nm compared to 700 nm for Design B. This peak value will be called Design C; the best design thus far within our limited search space. A simple calculation shows that, for a 10 mW internal signal power and laser drive current of 100 mA, 78 μW idler power can be generated within a 1 mm sample.

In passive structures without a QW, the PM wavelength can be accurately targeted, as we have reported in recent work [27]. In similar passive structures, the temperature tuning coefficient has also been extracted [28]. Indeed the tolerances of fabrication will be narrow and demanding; however, the PM wavelength can be influenced by the ridge width as well as the vertical structure [28,29]. In active devices, such as diode lasers, emission wavelength depends on the operating conditions. Changes in the optical properties in diode laser cavities have been studied previously and current injection is often the most significant cause of refractive index change. Bandgap changes due to temperature rise and band-to-band renormalization will also have an impact. They often manifest themselves at excessive injection levels. Accounting for all these effects is complex, but possible, as demonstrated by

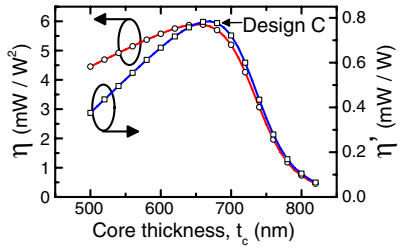

Fig. 9. (Color online) Variation of efficiencies η and η' with respect to core thickness. Here, the device length is $L = 1$ mm and the injected current is $I = 100$ mA.

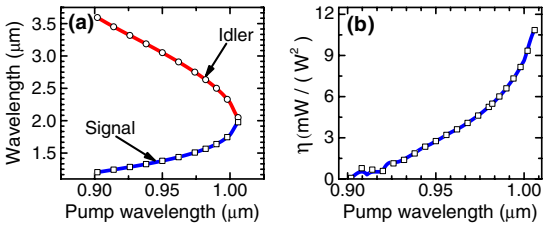

Fig. 10. (Color online) (a) Tuning of the phase-matched signal and idler wavelengths as the pump wavelength is varied. With decreasing pump wavelength, larger idler wavelengths are accessible, well past 3 μm. (b) Dependency of conversion efficiency on pump wavelength.

Shim *et al.* [30]. In that work, the authors describe the effect of injected carriers through a combination of the anomalous dispersion of three-dimensional carriers in the barrier and the free carrier plasma effect in the wells and in the barrier. In the case of the BRW structure, the effect of injected carriers in the intrinsically doped core region would also need to be included. As such, preliminary account for the temperature and carrier effects can be included into the calculations if desired. Once the vertical structure is fixed and grown, some tuning is still possible via the etch depth and ridge width.

Since wavelength tunability can be implemented using various methods [31,32], we have investigated the tuning characteristics of the phase matching attainable with these structures. By varying the pump wavelength, a set of phase-matched signal and idler wavelengths can be found by a zero-finding search (phase-matched wavelengths). The tuning curve for Design C along with the variation in η are shown in Fig. 10. From the figure, at shorter laser wavelengths, larger idler wavelengths are accessible. Also, the degeneracy point occurs for a longer laser wavelength at ≈1010 nm. The efficiency at these longer wavelengths also increases substantially due to better overlap of the interacting modes as they become similar in modal profile.

Table 2 compares the laser and nonlinear properties of designs A, B, and C. Design A has a relatively strong d_{eff}, comparable to the other designs. However, it has no value calculated for η and η' because the TIR mode reaches threshold well before the Bragg mode, making it a poor BRW laser. Design B is the most efficient laser of the three with lowest threshold and highest confinement factor. Its overall efficiency is worse than Design C due to smaller effective indices that reduce the nonlinear coupling coefficient, as described in Eq. (7d). Design C is the best overall device using the encompassing η' parameter because it takes into account both laser and nonlinear structural considerations. This exercise in optimization demonstrates the interplay of laser and nonlinear parameters and the route to optimizing the performance of such an integrated device.

4. OPTICAL PARAMETRIC OSCILLATION

This section will explore the possibility and requirements for parametric oscillation within these devices. Initially, only leakage losses will be included in the calculations such that their effect on OPO threshold can be minimized. Later in the section, other propagation losses will be included to obtain more realistic threshold values. The lossless parametric gain of a nonlinear element is described by [24]

$$g = \cosh(\Gamma_{\text{NL}} L), \tag{10a}$$

$$\Gamma_{\text{NL}} = \kappa \sqrt{P_p/(\lambda_s \lambda_i)}. \tag{10b}$$

When the gain equals the total cavity loss, oscillation can occur; this is the threshold condition. Two types of OPOs will be explored, namely, the singly resonant oscillator (SRO) and the doubly resonant oscillator (DRO). The threshold conditions for SRO and DRO are described as [24]

$$\text{SRO}: P_{p,\text{th}} = \frac{\lambda_s \lambda_i}{\kappa^2 L^2} [\cosh^{-1}(e^{\alpha_{s,t} L})]^2, \tag{11a}$$

$$\text{DRO}: P_{p,\text{th}} = \frac{\lambda_s \lambda_i}{\kappa^2 L^2} \left[\cosh^{-1}\left(\frac{e^{\alpha_{s,t} L} e^{\alpha_{i,t} L} + 1}{e^{\alpha_{s,t} L} + e^{\alpha_{i,t} L}} \right) \right]^2,$$
$$\alpha_{s,t} = \alpha_s - \ln(R_{s,1} R_{s,2}),$$
$$\alpha_{i,t} = \alpha_i - \ln(R_{i,1} R_{i,2}). \tag{11b}$$

Contour plots of threshold power as a function of sample length and core thickness are shown in Fig. 11 for (a) the case of SRO for the signal and (b) the case of DRO. Although most designs have very large CW threshold pump powers, some longer devices have more accessible requirements and can be achieved by existing single-mode diode lasers. For example, Design C with a cavity length of 3 mm has an SRO threshold of 978 mW. There are design challenges with such long laser lengths, such as decreased differential efficiency. Nonetheless, this demonstrates that BRW-ML-based OPO chips are possible and can be practically implemented with present day technology.

However, these ideal threshold values do not take into account practical losses, particularly absorption from dopants and scattering from structural roughness. These factors typically dominate the loss in ridge waveguide lasers. With respect to OPO thresholds, realistic signal and idler losses are needed, as seen in Eqs. (11a) and (11b). Since these wavelengths are

Table 2. Nonlinear Conversion Parameters for Three Phase-Matched BRW-ML Laser Structures[a]

	Design A $x_c = 0.1$ $d_c = 600$ nm	Design B $x_c = 0.45$ $d_c = 700$ nm	Design C $x_c = 0.45$ $d_c = 670$ nm
Γ_{BRW} [%]	0.51	1.24	1.14
I_{th} [mA]	279 (20.1 for TIR mode)	15.9	19.0
$A_{\text{eff}}^{(2)}$ [μm^2]	2603	306	272
d_{eff} [pm/V]	90.2	123.7	123.7
η [mW/(W · W)]	—	5.2	5.8
η' at 100 mA [mW/W]	—	0.72	0.78

[a]All designs have $L = 1$ mm, $x_1 = 0.15$, $x_2 = 0.40$ and $x_m = 0$.

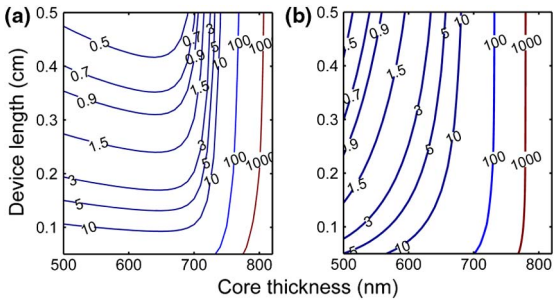

Fig. 11. (Color online) Contour plots of OPO threshold powers in watts for (a) signal SRO and (b) DRO as a function of core thickness and device length. The mirror reflectivities are 99.9% and 95% for both signal and idler.

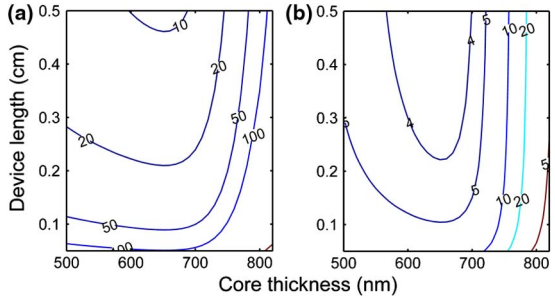

Fig. 12. (Color online) Contour plots of OPO threshold powers in watts for (a) signal SRO and (b) DRO as a function of core similar to Fig. 11. Here, signal and idler losses have been assumed to be 2 cm^{-1}.

far from the QW absorption band, the dopant contribution to absorption is negligible and only scattering is a major factor.

A more realistic value is 2 cm^{-1} for the TIR mode from a device tested using the Fabry–Perot technique for propagation loss at 1550 nm in a similar structure [33]. If the idler loss is assumed to be similar, then more realistic OPO thresholds can be estimated.

A similar contour plot is shown in Fig. 12. There are some notable differences between these thresholds and those in Fig. 11. First, the thresholds have all increased by at least 1 order of magnitude and there are no subwatt threshold OPOs. Second, the benefit of DRO OPOs can be seen in these higher loss scenarios as their thresholds are far lower than those of SRO OPOs. Here, the optimum configuration is for a 3–5 mm chip with 650 nm core width having threshold just over 4 W. In CW, these powers are difficult to obtain in single-mode lasers. Such pump powers can, however, be obtained as peak powers if the pump laser is mode locked. Nonetheless, it is important to note the effects of realistic propagation losses and not just leakage loss.

5. CONCLUSION

In conclusion, this paper has detailed the design strategy for efficient diode lasers based on BRW-ML structures that are phase matched for parametric oscillation. It has been shown that an effective method of integration is possible if the laser and nonlinear cavities are merged into one. The challenges of optimizing laser performance while maintaining phase matching are explored and detailed. It was shown that designing for optimized laser or nonlinear performance can lead to reduced overall conversion efficiency. A field transfer matrix approach has been utilized to calculate the various modal effective indices, as well as the propagation losses. These calculations and parameters are combined into a single parameter for efficiency of the complete laser and nonlinear conversion device, which can then be used for design optimization. The analysis was then used to examine parametric oscillation in both SRO and DRO OPO configurations; reasonable threshold values can be obtained if losses are reduced. It is expected that these structures can provide a suitable, flexible platform for portable, electrically driven, nonlinear conversion devices, such as OPOs and oscillators.

APPENDIX A: DERIVATION OF DIODE LASER OUTPUT POWER

Here we detail the derivation of Eq. (5), which estimates the output power of a diode laser from laser parameters. We begin with the output efficiency equation:

$$P_{\text{out}}(I) = (I - I_{\text{th}})\eta_d \frac{hc}{\lambda_p e}. \tag{A1}$$

We can note that the differential efficiency, η_d, is related to the internal quantum efficiency, η_i, by the following equation:

$$\eta_d = \eta_i \frac{\alpha_m}{g_{\text{th}}}, \tag{A2}$$

where α_m is the mirror loss and g_{th} is the threshold gain. Further, the current I can be converted to current density J via the relation $I = JLW$. This modifies Eq. (A1) to the following:

$$P_{\text{out}}(J) = \frac{LW\eta_i}{\lambda_p}(J - J_{\text{th}})\frac{hc}{e}\frac{\alpha_m}{g_{\text{th}}}. \tag{A3}$$

At threshold, the gain, g_{th}, is equal to the losses. Therefore, $g_{\text{th}} = \alpha_p L + \alpha_m$, where α_p is the propagation loss. The mirror loss can be further simplified by noting $\alpha_m = -\ln(R_{p,1}R_{p,2})$. Thus, Eq. (A3) becomes

$$P_{\text{out}}(J) = \frac{LW\eta_i}{\lambda_p}(J - J_{\text{th}})\frac{hc}{e}\frac{\ln(R_{p,1}R_{p,2})}{\ln(R_{p,1}R_{p,2}) - \alpha_p L}. \tag{A4}$$

Last, the threshold current density can be estimated by noting the net laser gain (above threshold) satisfies the following:

$$g_{\text{net}} = G_{\text{th}}\Gamma L = g_{\text{th}}. \tag{A5}$$

Further, the QW threshold gain, G_{th}, has a logarithmic relation with respect to transparency and threshold current densities:

$$G_{\text{th}} = G_0 \ln\left(\frac{J_{\text{th}}}{J_{\text{tr}}}\right). \tag{A6}$$

Using these, the threshold current density can be isolated:

$$J_{\text{th}} = J_{\text{tr}} \exp\left[\frac{\alpha_p L - \ln(R_{p,1}R_{p,2})}{G_0\Gamma L}\right], \tag{A7}$$

leading to the final result used to estimate the output power:

$$P_{\text{out}}(J) = \frac{WL\eta_i}{\lambda_p}\left[J - J_{\text{tr}}\exp\left(\frac{\alpha_p L - \ln(R_{p,1}R_{p,2})}{G_0\Gamma L}\right)\right] \times \frac{hc}{e}\frac{\ln(R_{p,1}R_{p,2})}{\ln(R_{p,1}R_{p,2}) - \alpha_p L}. \quad \text{(A8)}$$

REFERENCES

1. J. B. Khurgin, E. Rosencher, and Y. J. Ding, "Analysis of all-semiconductor intracavity optical parametric oscillators," J. Opt. Soc. Am. B **15**, 1726–1730 (1998).
2. J. Wang, J. Sun, Q. Sun, D. Wang, M. Zhou, X. Zhang, D. Huang, and M. M. Fejer, "Dual-channel-output all-optical logic AND gate at 20 Gbit/s based on cascaded second-order nonlinearity in PPLN waveguide," Electron. Lett. **43**, 940–941 (2007).
3. A. S. Helmy, P. Abolghasem, J. S. Aitchison, B. J. Bijlani, J. Han, B. M. Holmes, D. C. Hutchings, U. Younis, and S. J. Wagner, "Recent advances in phase matching of second-order nonlinearities in monolithic semiconductor waveguides," Laser Photon. Rev. **5**, 272–286 (2011).
4. A. De Rossi, V. Berger, M. Calligaro, G. Leo, V. Ortiz, and X. Marcadet, "Parametric fluorescence in oxidized aluminum gallium arsenide waveguides," Appl. Phys. Lett. **79**, 3758–3760 (2001).
5. A. S. Helmy, "Phase matching using Bragg reflection waveguides for monolithic nonlinear optics applications," Opt. Express **14**, 1243–1252 (2006).
6. J. B. Han, P. Abolghasem, B. J. Bijlani, A. Arjmand, S. Chaitanya Kumar, A. Esteban-Martin, M. Ebrahim-Zadeh, and A. S. Helmy, "Femtosecond second-harmonic generation in AlGaAs Bragg reflection waveguides: theory and experiment," J. Opt. Soc. Am. B **27**, 1291–1298 (2010).
7. P. Abolghasem, J. Han, B. J. Bijlani, A. Arjmand, and A. S. Helmy, "Continuous-wave second harmonic generation in Bragg reflection waveguides," Opt. Express **17**, 9460–9467 (2009).
8. J. Han, P. Abolghasem, B. J. Bijlani, and A. S. Helmy, "Continuous-wave sum-frequency generation in AlGaAs Bragg reflection waveguides," Opt. Lett. **34**, 3656–3658 (2009).
9. J. Han, P. Abolghasem, D. Kang, B. J. Bijlani, and A. S. Helmy, "Difference-frequency generation in AlGaAs Bragg reflection waveguides," Opt. Lett. **35**, 2334–2336 (2010).
10. Y. Li, Y. Xi, X. Li, and W. Huang, "A single-mode laser based on asymmetric Bragg reflection waveguides," Opt. Express **17**, 11179–11186 (2009).
11. B. J. Bijlani and A. S. Helmy, "Bragg reflection waveguide diode lasers," Opt. Lett. **34**, 3734–3736 (2009).
12. Y. Guowen, G. M. Smith, M. K. Davis, D. A. S. Loeber, M. Hu, C. Zah, and R. Bhat, "Highly reliable high-power 980 nm pump laser," IEEE Photon. Technol. Lett. **16**, 2403–2405 (2004).
13. R. W. Waynant, I. K. Ilev, and I. Gannot, "Mid-infrared laser applications in medicine and biology," Phil. Trans. R. Soc. A **359**, 635–644 (2001).
14. P. Yeh and A. Yariv, "Bragg reflection waveguides," Opt. Commun. **19**, 427–430 (1976).
15. P. Abolghasem and A. S. Helmy, "Matching layers in Bragg reflection waveguides for enhanced nonlinear interaction," IEEE J. Quantum Electron. **45**, 646–653 (2009).
16. T. Cunzhu, B. J. Bijlani, S. Alali, and A. S. Helmy, "Characteristics of edge emitting Bragg reflection waveguide lasers," IEEE J. Quantum Electron. **46**, 1605–1610 (2010).
17. B. R. West and A. S. Helmy, "Properties of the quarter-wave Bragg reflection waveguide: theory," J. Opt. Soc. Am. B **23**, 1207–1220 (2006).
18. J. Li and K. S. Chiang, "Guided modes of one-dimensional photonic bandgap waveguides," J. Opt. Soc. Am. B **24**, 1942–1950 (2007).
19. J. Chilwell and I. Hodgkinson, "Thin-film field-transfer matrix theory of planar multilayer waveguides and reflection from prism-loaded waveguides," J. Opt. Soc. Am. A **1**, 742–753 (1984).
20. H. C. Casey and M. B. Panish, *Heterostructure Lasers* (Elsevier, 1978).
21. S. Gehrsitz, F. K. Reinhart, C. Gourgon, N. Herres, A. Vonlanthen, and H. Sigg, "The refractive index of Al_xGa_{1-x} As below the band gap: accurate determination and empirical modeling," J. Appl. Phys. **87**, 7825–7837 (2000).
22. G. Aers, "Institute for Microstructural Sciences: National Research Council of Canada (NRC)," http://www.nrc-cnrc.gc.ca/eng/ibp/ims.html.
23. S. Dasgupta, A. Ghatak, and B. P. Pal, "Analysis of Bragg reflection waveguides with finite cladding: An accurate matrix method formulation," Opt. Commun. **279**, 83–88 (2007).
24. T. Suhara and M. Fujimura, *Waveguide Nonlinear-Optic Devices* (Springer 2003).
25. M. Ohashi, T. Kondo, R. Ito, S. Fukatsu, Y. Shiraki, K. Kumata, and S. S. Kano, "Determination of quadratic nonlinear-optical coefficient of AlGaAs system by the method of reflected 2nd harmonics," J. Appl. Phys. **74**, 596–601 (1993).
26. C. M. Kim, B. G. Jung, and C. W. Lee, "Analysis of dielectric rectangular waveguide by modified effective-index method," Electron. Lett. **22**, 296–298 (1986).
27. P. Abolghasem, J. Han, D. P. Kang, B. J. Bijlani, and A. S. Helmy, "Monolithic photonics using second-order optical nonlinearities in multilayer-core Bragg reflection waveguides," IEEE J. Sel. Top. Quantum Electron. **18**, 812–825 (2012).
28. B. J. Bijlani, P. Abolghasem, and A. S. Helmy, "Second harmonic generation in ridge Bragg reflection waveguides," Appl. Phys. Lett. **92**, 101124 (2008).
29. B. R. West and A. S. Helmy, "Analysis and design equations for phase matching using Bragg reflector waveguides," IEEE J. Sel. Top. Quantum Electron. **12**, 431–442 (2006).
30. J. Shim, M. Yamaguchi, P. Delansay, and M. Kitamura, "Refractive index and loss changes produced by current injection in InGaAs(P)-InGaAsP multiple quantum-well (MQW) waveguides," IEEE J. Sel. Top. Quantum Electron. **1**, 408–415 (1995).
31. L. A. Coldren, "Monolithic tunable diode lasers," IEEE J. Sel. Top. Quantum Electron. **6**, 988–999 (2000).
32. P. Abolghasem, M. Hendrych, X. J. Shi, J. P. Torres, and A. S. Helmy, "Bandwidth control of paired photons generated in monolithic Bragg reflection waveguides," Opt. Lett. **34**, 2000–2002 (2009).
33. P. Abolghasem, J. Han, B. J. Bijlani, A. Arjmand, and A. S. Helmy, "Highly efficient second-harmonic generation in monolithic matching layer enhanced $Al_xGa_{1-x}As$ Bragg reflection waveguides," IEEE Photon. Technol. Lett. **21**, 1462–1464 (2009).